

## ARTICLE OPEN



# Activity gradient driven mass transport in molten fluoride salt medium

Cody Falconer<sup>1</sup>✉, Mohamed Elbakhshwan<sup>2</sup>, William Doniger<sup>1</sup>, Matthew Weinstein<sup>2</sup>, Kumar Sridharan<sup>1,2</sup> and Adrien Couet<sup>1,2</sup>

The molten salt-cooled reactor concept has garnered significant interest and one of the current challenges limiting the deployment of these reactor concepts is the complex corrosion phenomenon observed in molten salt environments. One of these phenomena is activity gradient mass transport, which has been shown to affect dissimilar materials submerged in the same salt medium even when best efforts have been made to electrically isolate dissimilar materials from one another. This mechanism while shown experimentally, has not been predictively studied through a modeling approach. In this study, activity gradients in several 316L-X materials systems have been modeled and the mass transport predicted by the model has been confirmed through static isothermal corrosion testing in a molten fluoride salt medium.

*npj Materials Degradation* (2022)6:29; <https://doi.org/10.1038/s41529-022-00239-z>

## INTRODUCTION

Material compatibility with molten salts continues to be a limiting factor in the near-term deployment of high-temperature molten salt systems for future energy applications, such as the Generation IV molten salt cooled reactors<sup>1</sup>, thermal energy storage<sup>2</sup>, and concentrated solar power plants<sup>3</sup>. One of the most significant challenges revolves around understanding how materials corrode and interact with one another while submerged in molten salt. Typically, high-temperature materials are self-passivating and protect themselves from further corrosion through the formation of protective stable oxide layers<sup>4</sup>. However, in molten fluoride systems, oxide layers are fluxed away<sup>5</sup> leaving the alloy surface exposed to the salt environment enabling further corrosion.

One of the most common methods for materials degradation screening studies in salt environments has been the use of static isothermal corrosion test cells<sup>6,7</sup>, where sample material is submerged in static salt and held at a constant test temperature for a predetermined amount of time. However, these types of isothermal testing environments, although relatively simple in design, can create unique challenges that may affect the corrosion rates and mechanisms driving corrosion. A recent aggregation of the corrosion data in molten salts was performed by Raiman and Lee<sup>8</sup>, and showed that several design factors in a corrosion experiment can drastically change the corrosion performance of a tested alloy even when the same salt, test temperature, and test alloy are used. This prevents the establishment of reliable corrosion kinetics in given conditions and a deeper understanding of the corrosion phenomena. One of the factors that have been empirically shown to affect the corrosion rate is the choice of container material used in the design of a corrosion experiment<sup>8</sup>.

To date, the approach to choosing a corrosion testing container has been based on two approaches: (1) match the container material to the test material so that the risk of galvanic coupling is eliminated<sup>9</sup>, or (2) use a container material that is most likely to be thermodynamically inert in the molten salt<sup>10</sup>. The first approach is limited by the fact that not all materials can be processed as containers, and that not only the sample, but the container as well, will corrode, resulting in a larger sample surface area to volume of

salt ratio. This can rapidly saturate the salt with corrosion products, which would lead to an underestimation of the long-term corrosion rate. The second approach presents a situation where two dissimilar materials, with different standard redox potentials, exist in the same corrosive electrolyte. One of the most influential corrosion mechanisms between dissimilar materials is considered to be galvanic corrosion where an electrical connection is established between the dissimilar materials which create a galvanic current based on the differences in the materials corrosion potentials<sup>11</sup>. Because galvanic contact could influence the materials' corrosion rate, studies have used a ceramic strip to electrically isolate the two materials to effectively eliminate the galvanic couple<sup>12,13</sup>. Recent work, however, has shown that even when the galvanic coupling is eliminated, dissimilar materials still interact with one another with the occurrence of significant mass transport<sup>7,14</sup>.

This effect, although not clearly identified, has been hypothesized to be driven by an activity gradient between dissimilar materials and not electrical contact. In this work, computational tools are used to predict the activity gradient of elements in different materials in the same molten salt environment. Then corrosion studies are carried out to determine if elements are transported as predicted by the computed activity models. In addition, the effect of galvanic coupling is investigated by testing the dissimilar materials in both electrical contact and electrically insulated conditions.

## RESULTS

### Theoretical approach for activity gradient mass transport and materials selection

The activity gradient mass transport process effectively refers to how quickly the activity of an element in one material reaches the same activity level in the original material the element is transporting from. For brevity, it is simply referred to as an activity gradient in this study. It is hypothesized that this mass transport mechanism driven by activity gradients would not require electrical contact and instead be enabled by a

<sup>1</sup>Department of Materials Science and Engineering, University of Wisconsin-Madison, Madison, Wisconsin, USA. <sup>2</sup>Department of Engineering Physics, University of Wisconsin-Madison, Madison, Wisconsin, USA. ✉email: c.falconer@wisc.edu

disproportionation reaction of the corrosion products in the molten salt medium<sup>7,14,15</sup>. Some elements that are susceptible to corrosion in molten salts can be present in multiple oxidation states in the molten salt and therefore a disproportionation reaction must take place. Two important elements commonly used in high-temperature alloys that are susceptible to corrosion in molten fluoride salts are Fe and Cr, due to their negative metal fluoride-free energies of formation. There is evidence that Fe and Cr can also be disproportionate by reaction (1) and have multiple oxidation states<sup>16,17</sup>.



Here  $M$  represents a metal, such as Fe or Cr, and the subscripts  $d$  and  $s$  indicate either a dissolved or solid species. Ozeryanaya<sup>15</sup> and Olson et al.<sup>14</sup> speculated that the disproportionation reaction would be driven electrochemically and would occur on the surface of a material such that an adsorbed atom,  $M_s$ , is formed. Based on the chemical potential of this atom at the surface, it can then form a compound (Olson et al.<sup>14</sup>), an intermetallic, or a solid solution (Falconer et al.<sup>7</sup>) with the substrates' elements. Wang et al.<sup>18</sup> and Peng et al.<sup>19</sup> also demonstrated that the disproportionation of  $CrF_2$  into  $CrF_3$  and Cr occurred in LiF-NaF-KF (FLiNaK) salt without the need of a surface to promote the reaction, which would lead to dissolved metallic Cr in the FLiNaK salt. The dissolved metal would then transport to the surface of other material submerged in the salt via a chemical potential gradient. This disproportionation reaction provides an electrochemically driven pathway for elements to transport from one material to another in FLiNaK salt without the need for electron transfer via electrical contact (i.e. galvanic coupling) to promote transport. This activity gradient transport mechanism enabled by electrochemical reactions would be unique to molten salt since even elements with relatively low solubility in the salt could significantly transport through the system. This is analogous to the well-known chemically (i.e. solubility) driven transport mechanism of Ni or C in liquid Na metal, for instance, where the elemental metal solubility in the liquid metal is the main driver for material degradation<sup>20,21</sup>. In a previous study<sup>7</sup>, the authors investigated the effect of galvanic coupling on corrosion by testing Ni-201 samples suspended in molten FLiNaK salt at 700 °C contained in a 316L stainless steel (henceforth referred to as 316L) capsule with and without electrical contact. It was found that in both cases Fe and Cr would transport from the 316L capsule to the Ni-201 samples. In addition, it was found that the electrical contact had little to no effect on the amount of Fe and Cr that was transported. The authors concluded that the Fe and Cr activity gradients from the 316L to the Ni-201 resulted in mass transport. However, that hypothesis was not properly validated by targeted experiments. The work presented in this study uses computational methods to predict material combinations that will affect the activity gradient observed in our previous work<sup>7</sup>, with the hypothesis that by choosing dissimilar materials that reduce, or effectively eliminate the elemental activity gradient, mass transport can be substantially mitigated.

For the purposes of modeling the activity gradients in this study, one material susceptible to corrosion in FLiNaK salt was chosen, such that corrosion products susceptible to disproportionation would dissolve into the molten FLiNaK. For this reason, 316L was chosen as it contains Cr and Fe which are susceptible to corrosion in FLiNaK due to their large negative Gibbs free energies of formation of their fluoride compounds<sup>17</sup>. In addition, Cr and Fe are also susceptible to disproportionation.

With 316L chosen as one material, the choice of the other materials now dictates how large the elemental activity gradient is. Furthermore, the second material must be more resistant to corrosion than 316L in FLiNaK, to prevent any risks of corrosion product saturation in the salt or additional contaminants that

could affect transport. In addition to the Ni-201 used previously<sup>7</sup>, materials had to be identified that would alter the activity gradients for Cr and Fe while remaining resistant to corrosion in FLiNaK salt.

To identify the elements that would be expected to be more resistant to corrosion in FLiNaK salt than 316L, HSC Chemistry 7.22 software was used to determine Gibbs free energies of formation for fluoride compounds for all the elements available in the PanHEA<sup>23</sup> and PanNickel<sup>24</sup> thermodynamics databases.

The Gibbs free energy of formation for fluorides are reported in Fig. 1a. Since 316L is an Fe-based alloy, only the elements with higher (less negative) free energies of fluoride formation than Fe (solid lines) were considered; these elements were Sn, Co, Ni (already selected based on the previous work<sup>7</sup>), W, Mo, Cu, C, Ag, Pt, and Au. Of these elements, Sn was not considered due to its low melting temperature of 232 °C. In addition, C was not considered as graphite has been used in many corrosion experiments in the past and has already been shown to interact with corrosion products that enter FLiNaK salt<sup>14,25</sup>. With this initial material screening approach only Co, Ni, W, Mo, Cu, Ag, Pt, and Au were identified for further analysis.

Pandat software<sup>26</sup> was then used to investigate the activity gradients that may exist in a 316L-X system where X is either Co, Ni-201, W, TZM (titanium-zirconium-molybdenum alloy), Cu, Ag, Pt, or Au. Note that Ni-201 was used instead of pure Ni because of the previous study<sup>7</sup> and TZM was used instead of pure Mo because TZM contains 99.4% Mo and has better high-temperature strength than pure Mo suggesting that TZM is more likely to be used in a high-temperature molten salt system<sup>27</sup>.

In Fig. 1b the activity of the main alloying elements in 316L are plotted as a function of temperature. As expected, the activities rank as the weight fraction of each element in 316L. Fe has the highest activity as it is the primary element in 316L followed in concentration and activity level by Cr. The lower trend in the Ni activity is a result of the high solubility of Ni in the FCC austenite phase. On the other hand, Mo is BCC, but Mo exists in an FCC phase as well as several intermetallic phases in 316L<sup>28</sup> which is the reason it has such a high activity even at low concentrations. The activity values of Cr and Fe at 700 °C, the chosen isothermal corrosion test temperature, are most important for comparison since Fe and Cr are electrochemically active, and are equal to 0.55 and 0.72, respectively. These activity values for Cr and Fe were treated as a threshold value for evaluating the activity gradient for Cr and Fe in each of the possible 316L-X couple test systems to determine which test systems would most likely provide a desirable activity gradient.

To determine the activity gradient for Cr and Fe in each of the possible 316L-X couple test systems, the activity of Cr and Fe were calculated and plotted as a function of either increasing Cr or Fe concentration in the X material. An example of Ni-201 is given in Fig. 1c, d for Cr and Fe, respectively. The left-most data point in both plots corresponds to the nominal composition of Ni-201. As the concentration of either Cr or Fe increases, the concentrations of the remaining elements in Ni-201 decrease uniformly. The concentration at which point the activity of either Cr or Fe is equal to the activity of Cr and Fe in 316L (i.e., where the activity gradient is zero) was set as the threshold concentration. These threshold values are indicated by a red dashed line in Fig. 1c, d. Initially, a large activity gradient does exist for the Cr and Fe activities in 316L to the activities of Cr and Fe in Ni-201. The threshold concentration for Cr and Fe in Ni-201 are as high as 25 wt% and 65 wt%, respectively, suggesting that both Cr and Fe could undergo significant mass transport before the activity gradient becomes negligible and transport would stop. This was indeed observed by Falconer et al.<sup>7</sup>. The same modeling approach was performed for all of the materials identified as X and the threshold concentrations are reported in Fig. 1e, f. Additional activity plots for all materials identified as X can be found in Supplemental

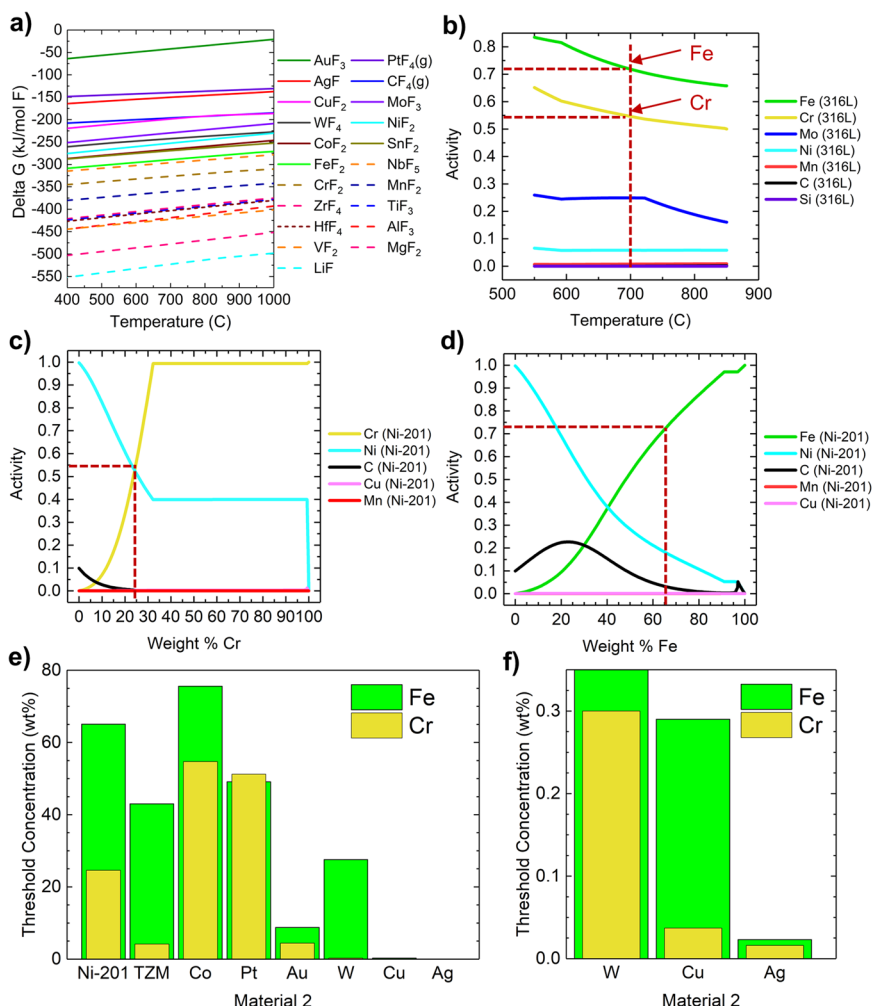


**Fig. 1 Results for fluoride formation energy and activity calculations.** **a** Fluoride formation energies calculated using HSC V.7.00<sup>22</sup>. **b** Activities of main alloying elements in 316L. **c, d** Activity of Cr and Fe, respectively, as functions of increasing weight % in Ni-201. **e** Fe and Cr threshold concentration plots for all second materials. **f** Zoomed in threshold concentration plot to better show threshold concentrations in W, Cu, and Ag material.

Materials. In each of these plots, it can be observed that regions of nearly constant activity exist. For example, in Fig. 1c, in the composition range of approximately 30 wt% to 99 wt% Cr, the activity of Cr and Ni are constant. These regions correspond to multiple phase fields where the phase fractions rather than the elemental activities vary as a function of compositions. For Fig. 1c, at about 30 wt% Cr, the Ni-rich single-phase FCC reaches maximum Cr solubility and separates into a BCC phase that nearly only contains Cr, hence an activity approaching unity, while Ni remains in an FCC phase with the remaining elements.

From the plots of threshold concentration, three possible activity gradient trends can be noted. First, a large initial activity gradient for both Cr and Fe is possible if either Ni-201, Co, or Pt are used in the 316L-X test couple. Second, a large gradient for Fe and a small gradient of Cr exists if either TZM or W are present in the 316L-X test couple. Finally, no significant gradient exists for either Cr or Fe if Au, Cu, or Ag are used in the 316L-X test couple. The first trend has been tested by Falconer et al.<sup>7</sup>, however, testing of the remaining activity gradient combinations to validate the approach has not been performed in the literature. From these activity gradient modeling results, two materials were chosen to test if the activity gradient would drive the mass transport in molten salt. TZM was selected over W for the strong Fe gradient and low Cr gradient as TZM has garnered interest in the molten salt community for protective claddings<sup>6</sup>. In terms of actual

engineering feasibility, Cu was determined to be the best choice over Au and Ag on account of cost for the case of no gradient for either Cr or Fe.

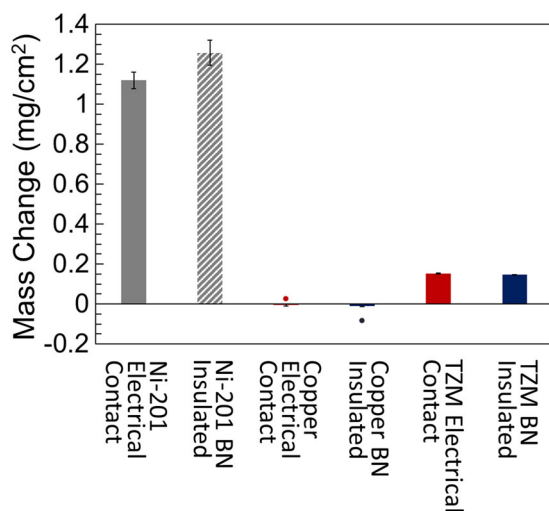
### Experimental results

To observe any changes in the elemental concentrations in the FLiNaK salt, pre- and post-corrosion salt samples were analyzed using the ICP-MS method. The results are reported in Table 1. The as-received FLiNaK has low concentrations of all metal impurities considered important in this study. After 500 h exposure at 700 °C, however, several changes in the elemental concentrations occur. As expected from the corrosion of the 316L capsule, the concentration of Cr increases in all the corrosion capsules as does the concentration of Mn. Both elements have very negative free energies of formation for their respective fluoride compounds and are known to be the elements most susceptible to dissolution in 316L<sup>29</sup>. Zr and Ti, minor alloying elements in TZM where compositions are <0.5 wt%, also have very negative free energies of formation for their respective fluoride compounds<sup>10</sup>, but the concentrations in the post-corrosion salts do not change significantly. The concentrations of elements considered resistant to corrosion in fluoride salts, Mo and Ni, decrease in the post-corrosion salts. Finally, the concentration of Fe also decreases in all the post-corrosion salt samples.

**Table 1.** ICP-MS results for the as-received FLiNaK and post-corrosion FLiNaK.

Sample	Fe	Cr	Mn	Ni	Cu	Mo	Zr	Ti
As-received FLiNaK	15 ± 0.8	3.9 ± 0.2	0.5 ± 0.05	5.0 ± 0.3	0.2 ± 0.02	1.1 ± 0.1	1.0 ± 0.08	1.2 ± 0.3
TZM electrical contact	3.5 ± 0.2	317 ± 33	22 ± 0.9	0.2 ± 0.04	0.09 ± 0.02	0.08 ± 0.02	0.6 ± 0.06	0.7 ± 0.1
TZM BN insulated	2.6 ± 0.2	331 ± 49	25 ± 1.4	0.2 ± 0.04	0.1 ± 0.01	0.08 ± 0.02	0.7 ± 0.1	1.3 ± 0.1
Copper electrical contact	4.1 ± 0.2	257 ± 27	19 ± 0.8	0.3 ± 0.04	0.4 ± 0.03	0.1 ± 0.02	1.5 ± 0.1	1.0 ± 0.07
Copper BN insulated	10.6 ± 0.5	269 ± 28	21 ± 0.9	0.2 ± 0.03	1.3 ± 0.07	0.06 ± 0.01	0.7 ± 0.07	12.4 ± 0.7

Reported units are in µg/g (wt ppm).

**Fig. 2** Post-corrosion mass change results. TZM and copper results from this study are plotted along with results from Falconer et al.<sup>7</sup> shown in gray for comparison to the Ni-201 sample sets studied in their experiments. Error bars are standard deviations between samples.

As a first assessment of mass transport, the post-corrosion masses of TZM and copper were measured and the mass change per area was calculated. The results are shown in Fig. 2. One copper sample from each of the tests appeared to be outliers and are plotted as individual points. Also plotted in Fig. 2 are the mass change results of the Ni-201 sample sets studied by Falconer et al.<sup>7</sup> Falconer et al. observed a significant increase in the mass of both Ni-201 sample sets, and this mass increase was attributed to the mass transport of both Cr and Fe from the 316L corrosion capsules to the Ni-201 samples.

In this study, it was predicted that due to the activity gradient of Fe between 316L and TZM, the mass transport of Fe would occur from the 316L to the TZM samples resulting in a mass gain after corrosion tests. Alternatively, little to no change in the copper sample's mass was expected because of the lack of an activity gradient for either Fe or Cr between 316L and the copper samples and the relatively positive free energy of fluoride formation of Cu. The post-corrosion mass measurements partially confirmed both predictions with the TZM samples gaining mass during corrosion tests, although no information on what elements transported are revealed by mass change, and little to no change is observed in the copper samples.

The XRD analysis of TZM and copper sample sets is presented in Fig. 3a, b, respectively. In Fig. 3a, both TZM samples appear to have similar new phases as evidenced by new peaks in the XRD spectrum. Several of the new peaks were matched with a  $M_6C$  phase (PDF 01-083-3017) with a stoichiometry of  $Fe_3Mo_3C$ . In addition, at least two peaks present in the XRD spectrum could

not be matched to the  $M_6C$  phase. According to the binary phase diagram of Fe and Mo, two possible intermetallic compounds between Fe and Mo are possible at the test temperature of 700 °C<sup>30</sup>. The database used to match the peaks only contained one possible stoichiometry of the  $\mu$ -phase ( $Fe_3Mo$ ; PDF 00-031-0641). This stoichiometry of the  $\mu$ -phase matched only one of the unidentified peaks. In addition,  $\alpha$ - $Mo_2C$  (PDF 00-035-0787) appeared to match both the unidentified peaks.

The XRD patterns of the copper samples show no evidence of new phases being present on the samples after exposure to the FLiNaK salt. However, after being exposed to the test temperature of 700 °C for 500 h there is a clear sign of grain growth as evident by the preferential diffraction (see for instance (200) relative to (111) peaks), and suppression of other characteristic FCC peaks. A 2 mm diameter collimator was used during the analysis without sample rotation, which would explain why a more random distribution of diffracted grains was not observed.

To evaluate surface roughening and precipitation of new phases on the sample surfaces, SEM with EDS analysis was performed. The planar SEM/EDS analysis for the TZM sample in electrical contact with the 316L, and the TZM sample that was BN insulated from the 316L capsule are shown in Fig. 4a, b, respectively. In addition, EDS point analysis was performed in several regions of each sample and is reported in Table 2. In both TZM samples, the surface is decorated with a thin film of nanometer-sized precipitates which is believed to be the carbide phase appearing in the XRD measurements shown in Fig. 3a. Due to the size of the precipitates, true quantitative measurements of the elements in each region cannot be made because of the interaction volume of the electron beam. However, qualitatively the concentration of elements in regions with a high density of precipitates and the matrix (points 1, 2, 5, and 6 in Table 2 correspond to matrix) appears to differ by a few atomic percent. In the matrix, Mo and Zr concentrations are relatively reduced while the concentrations of Fe and Cr are relatively elevated.

In addition to the surface SEM/EDS analysis, cross-sections (XS) of the TZM samples were also characterized to observe if elements from the 316L had diffused into the near surface region of the samples. The cross-sectional analysis of the TZM sample in electrical contact with the 316L corrosion capsule and the TZM sample BN insulated from the 316L corrosion capsule are shown in Fig. 4c, d, respectively. Note that the Cu coating on the surface of each sample was deposited post-corrosion for edge retention during the metallographic preparation. Both samples show almost identical results. From the secondary electron images, a thin layer with a faint change in contrast can be seen in between the Cu coating and the bulk TZM samples. EDS mapping reveals that this region contains a relatively high concentration of Fe and smaller concentrations of Cr. This thin layer likely corresponds to the intermetallic layer and possible carbide revealed by the XRD analysis in Fig. 3a. The Cr and Fe appear to only be present right at the sample surface with little to no diffusion into the bulk of the TZM sample suggesting that the carbide/intermetallic layer may act as a diffusion barrier for Fe and Cr.

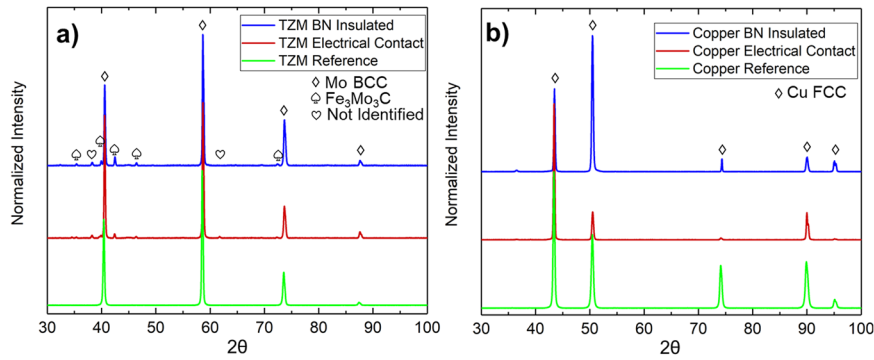


Fig. 3 XRD analysis on the TZM and copper sample sets. **a** TZM. **b** Copper.

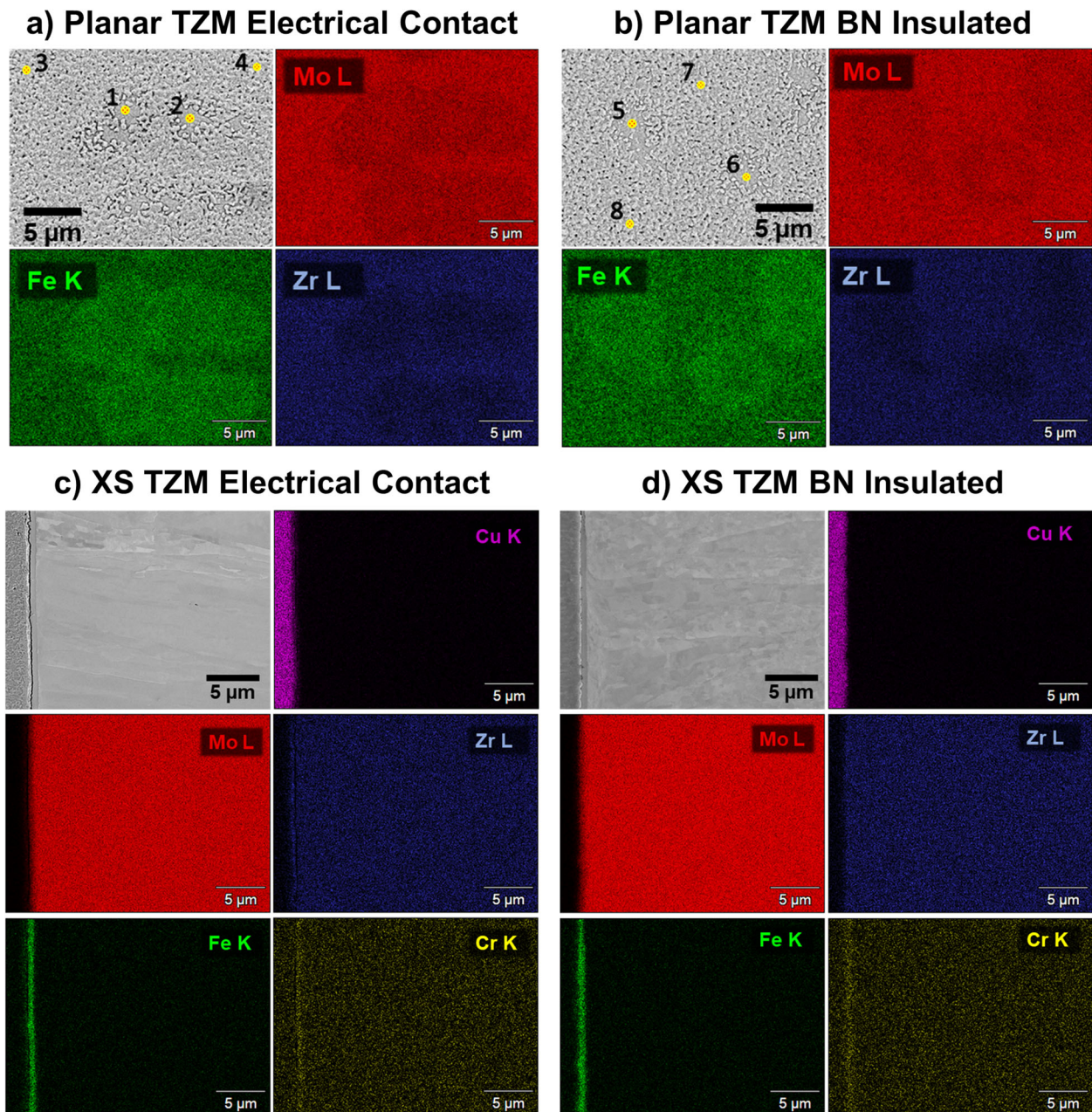


Fig. 4 SEM/EDS analysis of TZM. **a, b** Planar analysis performed on the salt facing surface of the TZM sample held in electrical contact with the 316L-SST capsule and the sample BN insulated from the 316L-SST, respectively. **c, d** Cross-sectional (XS) analysis of the sample held in electrical contact with the 316L-SST capsule and the sample BN insulated from the 316L-SST capsule, respectively.

**Table 2.** EDS point analysis performed on the planar TZM samples.

Point	Cr K	Fe K	Ni K	Zr L	Mo L
<i>Electrical contact</i>					
1	4.45 ± 0.21	42.33 ± 0.46	0.20 ± 0.16	1.11 ± 0.09	51.46 ± 0.31
2	4.16 ± 0.21	42.05 ± 0.46	0.26 ± 0.16	1.11 ± 0.09	51.97 ± 0.31
3	3.73 ± 0.23	38.90 ± 0.49	0.00 ± 0.00	1.65 ± 0.22	55.19 ± 0.40
4	3.60 ± 0.13	37.54 ± 0.49	0.11 ± 0.18	1.59 ± 0.23	56.73 ± 0.41
<i>BN insulated</i>					
5	3.51 ± 0.22	38.23 ± 0.48	0.34 ± 0.17	1.36 ± 0.10	56.09 ± 0.34
6	3.91 ± 0.22	38.55 ± 0.47	0.10 ± 0.17	1.33 ± 0.10	55.54 ± 0.34
7	3.83 ± 0.23	36.87 ± 0.49	0.00 ± 0.14	2.31 ± 0.23	56.67 ± 0.41
8	3.24 ± 0.24	35.93 ± 0.50	0.24 ± 0.18	2.24 ± 0.24	58.11 ± 0.42

Points correspond to those labeled in Fig. 4.

Data generated by Pathfinder EDS software v.2.4 and reported units are in atomic%.

Even though the XRD analysis in Fig. 3b did not reveal any obvious new phase formation on the surface of the copper samples, planar SEM/EDS analysis was also performed on both the copper sample in electrical contact with the 316L capsule and the copper sample that was insulated from the 316L capsule with BN. In Fig. 5a, b, it can be observed that the surfaces of both copper samples are now decorated with large globular-shaped precipitates as well as nanometer-sized particles. The large globular precipitates are only present in various sized patches throughout the surface of the sample and appear to have high concentrations of both Cr and Fe from the corrosion of 316L capsule. The globular precipitates appear to be deposited on the surface and not fully embedded in the surface, suggesting that these precipitates may have formed during the cooling process during the termination of the corrosion tests in the FLiNaK salt. Further evidence of this is seen in the potassium K map in Fig. 5a. A large potassium-rich particle clearly exists on the surface and is most likely a particle of salt that was not removed during the post-corrosion cleaning process.

Cross-sectional analysis of the copper sample in electrical contact with the 316L capsule and the sample that was BN insulated from the 316L capsule were also investigated, but not presented as they did not display elemental transport and diffusion as predicted by the lack of mass change, data shown in Fig. 2. Neither copper sample showed additional elements in the near-surface region of the cross-section. EDS line scans only revealed pure Cu in both the copper sample electrically connected to the 316L capsule and the copper sample that was BN insulated from the 316L capsule.

To evaluate elements in concentrations lower than what EDS can reliably detect, the copper samples surfaces were also analyzed using XPS. Figure 5c shows the XPS spectra for the elements of interest that were expected to transport through the salt. The surface signal is dominated primarily by Cu and shows some signs of Cu oxidation after salt exposure. The scans from the *Mn2p* and *Fe2p* binding energy ranges show that faint Mn and Fe signals are observed and that they correspond to the unexposed copper reference sample and persist after exposure to molten salt. In addition, the scan over the *Cr2p* energy range shows no evidence of significant Cr transport. The peak observed at a binding energy of 570 eV is characteristic of the *CuLMM* peak and comes from the copper sample<sup>31,32</sup>. The XPS data suggests that there is limited to no elemental transport and diffusion of elements from the 316L corrosion capsule to the copper samples regardless of the electrical contact condition.

## DISCUSSION

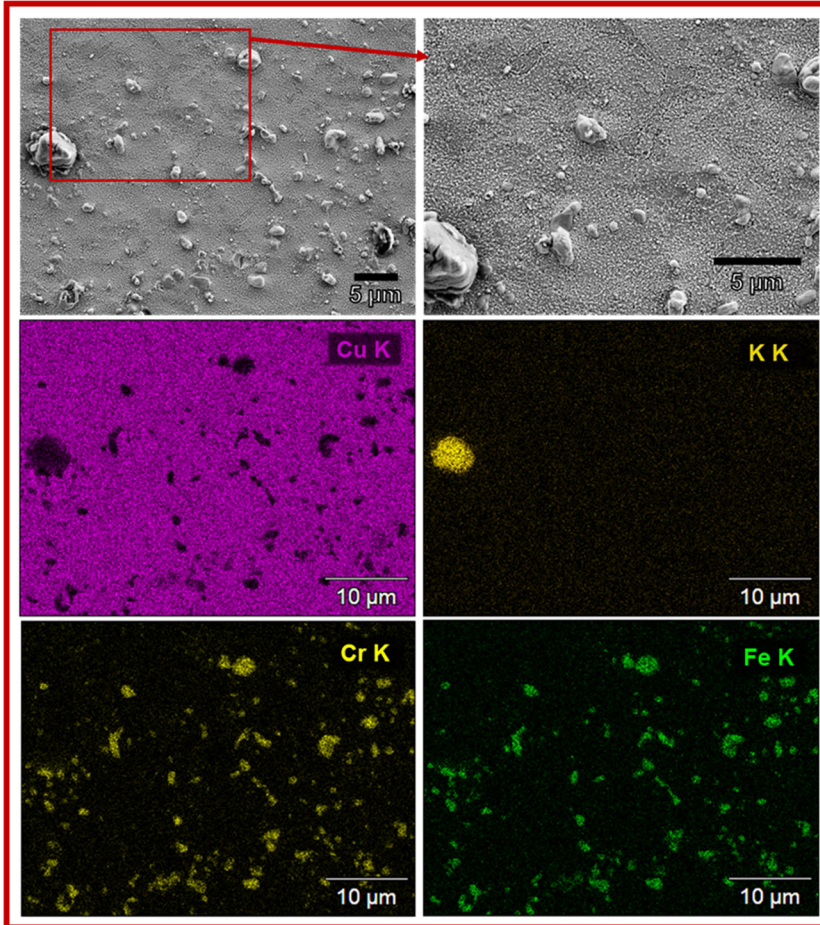
Previous studies between dissimilar materials submerged in molten salt media have shown that the mass transport between materials does not require electrical contact and the most likely mechanism underlying the mass transport is a result of activity gradients between the elements in each material coupled to an electrochemically active element via electrochemical and disproportion reactions<sup>7,14,15</sup>. The primary goal of this work was to investigate the feasibility of using computational methods to predict activity gradients between dissimilar materials submerged in the same molten salt medium and then investigate whether the elements transported match the predictions calculated by activity gradients. At first, activity gradients were modeled in a dissimilar material system already studied experimentally in literature<sup>7</sup>. Falconer et al.<sup>7</sup> observed a significant transport of Fe from 316L to Ni-201. They also observed the transport of Cr to a lesser degree than Fe. From the activity modeling performed in this study, the transport behavior in Falconer et al.'s study was accurately predicted. From Fig. 1c, d an activity gradient for both Cr and Fe exists in the 316L Ni-201 system. In addition, the activity gradient for Fe is much larger than that of Cr suggesting a higher driving force for the transport of Fe as observed experimentally<sup>7</sup>.

In this study, TZM was selected as the sample material because of interest in this alloy to the molten salt community. The activity gradient modeling in this case showed that only a significant gradient for Fe existed, while the gradient for Cr was small. From this result, the mass transport behavior of TZM should result in mostly Fe transport between 316L and TZM, while the transport of Cr would be greatly reduced or not observed at all. From the SEM/EDS results shown in Fig. 4, it can clearly be seen that the transport of Fe was far more significant than that of Cr as predicted by the threshold concentrations reported in Fig. 1e.

The final corrosion system studied was copper samples in 316L capsules. Copper was selected as the sample material because it has very limited solubility of both Fe and Cr and additionally, does not form any intermetallic compounds with Fe or Cr. It was believed that the activity gradient between the Cr and Fe that exists in 316L and the Cr or Fe that could exist with copper would therefore be non-existent leading to limited to no transport of Cr or Fe to the copper samples. Once again, from the experimental results presented in Fig. 5, the activity gradient modeling was able to accurately predict the lack of elemental transport in this material couple system. Furthermore, the activity modeling and experimental work performed here shows that by selecting alloy combinations that effectively eliminate the activity gradient, mass transport between materials in the same salt medium can be reduced or even prevented completely.

Finally, in addition to the activity (i.e. thermodynamics) considerations, an important part of the transport mechanism is the diffusion behavior (i.e. kinetics) of the Fe and Cr in the second material. As Fe and Cr deposit on the second material, the salt-facing surface concentration changes. Therefore, the extent of the activity gradient between the Fe and Cr in 316L and the Fe and Cr at the surface of the second material will be reduced. As observed by Falconer et al.<sup>7</sup>, Fe and Cr diffuse relatively quickly into Ni-201 such that the surface concentrations of Fe and Cr do not reach their threshold concentrations. Hence while a significant amount of Cr and Fe is transported, the system remains far away from thermodynamic equilibrium. In addition, because of the existence of a diffusion profile in Ni-201, the limiting factor for the transport would eventually be the diffusion of Cr and Fe into the Ni-201 and not the diffusion through the molten salt. A different situation is observed in the TZM sample. Since the transported Fe forms an intermetallic compound at the surface of the TZM, the Fe surface concentration is close to the threshold concentration, limiting the driving force for transport. In addition, because of the relatively

### a) Copper Electrical Contact



### b) Copper BN Insulated

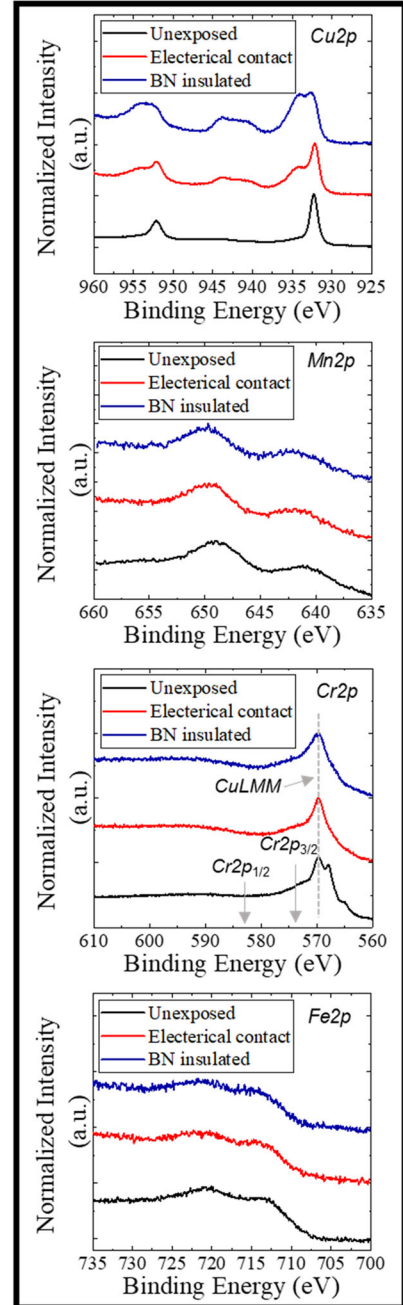
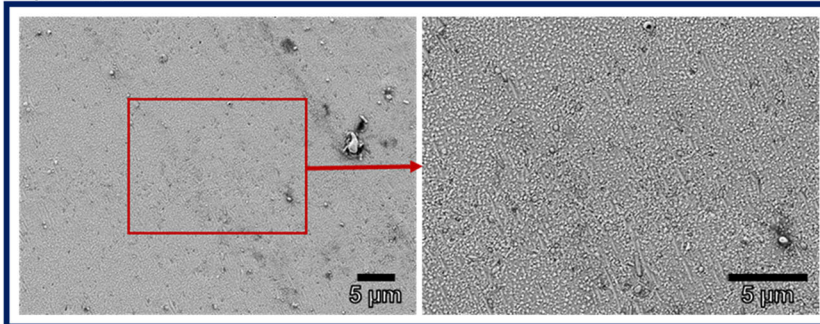


**Fig. 5 SEM and XPS analysis of copper samples.** **a** Planar SEM images with EDS maps of the copper sample in electrical contact with the 316L corrosion capsule. **b** Planar SEM images of the copper sample electrically insulated from the 316L corrosion capsule. **c** XPS binding energy plots from both exposed copper samples were plotted with the unexposed copper sample for comparison.

low diffusion coefficient of Fe in the Fe-Mo intermetallic<sup>33</sup>, the Fe transport in TZM is kinetically limited.

The mechanism driving the activity gradient mass transport of Fe and Cr occurs in two steps. The first step is a general corrosion reaction. Fe and Cr dissolve into the salt as corrosion products. Due to the fluorobasic nature of the FLiNaK salt<sup>34</sup> both Fe and Cr can form corrosion products where Fe and Cr are in their 2+ and 3+ oxidation states. The negative Gibbs free energy of formation for both fluoride compounds strongly suggests that Fe and Cr are susceptible to dissolution through reactions at the 316L corrosion

capsule surface:



These reactions proceed, producing  $MF_{2(d)}$  and  $MF_{3(d)}$ , until all the free fluoride or impurities in the salt are consumed. In step two, the second part of the activity gradient transport mechanism

occurs, namely the disproportionation reaction shown in reaction (1). Disproportionation can either take place on a surface, if the formation of  $M_s$  is favorable (the surface acts as a catalyst) resulting in the formation of a solid solution or compound, or reaction (1) can occur in the FLiNaK salt leading to the creation of  $M_d$ .  $M_d$  will then form a solid solution or intermetallic compound with another material submerged in the salt following a chemical potential driving force. This mechanism does not require the two materials to be in electrical contact with one another and in fact, electrical contact appears to play little to no role in changing the behavior of the mass transport.

Based on the results reported in this study and by Falconer et al.<sup>7</sup>, the primary factors that appear to significantly affect the mass transport behavior is the presence of an elemental activity gradient between two materials in the salt medium, coupled to (i) that element dissolving electrochemically in the salt from material 1, (ii) that element being susceptible to a disproportionation reaction either in the salt or at the surface of material 2 and (iii) a non-negligible diffusion coefficient of that element in material 2. Of the three material combinations, the 316L-Cu system appears to be the most resistant to mass transport driven by activity gradients due to the lack of an activity gradient that could lead to significant mass transport of Fe and Cr to Cu.

Other high-temperature alloys such as Ni-based alloys may not be as resistant to mass transport in the presence of copper because Cu and Ni readily form a solid solution with one another<sup>35</sup>. This could mean that the activity gradient between the Ni in a Ni-based alloy and the Ni in copper could lead to significant mass transport.

The performance of the copper samples in this study also indicates that copper and its alloys are materials that warrant further study in molten salt media. The high operating temperatures of a molten salt reactor (up to 700 °C) eliminate pure copper from being used as a structural material. However, copper coatings could be of interest and Cu-coated 316H has been shown to have excellent corrosion resistance in molten FLiNaK<sup>36</sup>.

## METHODS

### Elemental activity modeling in pandat

The Pandat software calculates activities by performing Gibbs free energy minimization to find the stable state using the thermodynamic data from a database<sup>37,38</sup>. For the calculations in this study both the PanHEA<sup>23</sup> and PanNickel<sup>24</sup> databases were used. In addition, the user must assign a reference phase to each component in the material system. For the element's activities modeled, the reference phase chosen was the one most stable at room temperature as reported in Table 3.

### Salt and material preparation

The FLiNaK (46.5% LiF, 11.5% NaF, and 42% KF, in mol %) salt used in this study was pre-mixed and melted by Materion Corporation. The salt was prepared in graphite crucibles using at least 99.9% pure LiF, NaF, and KF. Additional details on the FLiNaK used and how it was handled have been reported previously<sup>7</sup>.

TZM material was procured from H.C. Stark, Cleveland, OH. The material was produced by arc casting and subsequently cut into 17.8 mm × 10.2 mm × 2 mm samples with two 1.7 mm holes drilled into each side. To make copper samples, a 19 mm × 9.5 mm rectangular bar of copper alloy C110 (referred to simply as copper through this manuscript) was procured from a commercial vendor and 1.8 mm thick samples were sectioned off using a high-speed saw. After sectioning, two 1.5 mm holes were drilled into each sample to allow for suspending the samples in molten salt. The nominal compositions of the TZM and C110 alloy used in this study are shown in Table 4. All TZM and copper samples were ground to a 1200 grit surface finish using SiC abrasive paper following which they were ultrasonically cleaned with deionized water and acetone. The dimensions and masses of each sample were measured and recorded before suspending the samples. Two sets of two TZM samples were suspended using pure Mo wire while two sets of three copper samples were suspended using copper wire. All four sample strings were then transferred

**Table 3.** List of reference phases used for each element in the activity modeling in Pandat.

Element	Reference phase
C	Graphite
Cr	BCC
Fe	BCC
Mn	CBCC_A12
Mo	BCC
Ni	FCC
Si	Diamond
Cu	FCC
Zr	HCP
Ti	HCP

**Table 4.** Nominal composition of the TZM and copper alloy C110 used to prepare samples.

Sample Material	Cu	Mo	Zr	Ti	C
TZM	–	99.2 min	0.08 max	0.50 max	0.04 max
C110	99.99	–	–	–	–

Units are mass%.

into an ultra-high purity argon atmosphere glovebox for exposure to molten FLiNaK salt.

316L stainless steel capsules were prepared from 316L tubing 127 mm in length with a 25.4 mm outer diameter and 2.1 mm wall thickness. To create a capsule, one end of the tubing was sealed with a 316L plug machined from round stock and welded onto the tube using gas tungsten arc welding (GTAW). Additional details on the capsule preparation have been reported previously<sup>7</sup>.

Two sets of two TZM samples were tested while two sets of three copper samples were tested using either a 316L cap so that the samples and the 316L corrosion capsule were galvanically connected or electrically insulated with a boron nitride (BN) cap. A diagram showing the corrosion capsule system and sample placement is shown in Fig. 6.

### Experimental system

All salt preparation was performed inside an ultra-high purity argon glovebox. 316L corrosion capsules were filled with 70 grams of FLiNaK salt. The salt volume was calculated assuming the FLiNaK density correlation reported in Williams et al.<sup>34</sup>. With this correlation, the ratio of exposed-metal surface area to volume of salt was calculated to be approximately 2 cm<sup>-1</sup> for the 316L corrosion capsule and approximately 0.4 cm<sup>-1</sup> and 0.3 cm<sup>-1</sup> for the copper and TZM sample sets, respectively. Once the salt was loaded into the 316L corrosion capsules, the capsules were placed in a furnace at 700 °C inside the glovebox to allow the salt to melt. The samples were then introduced into the molten salt at the test temperature of 700 °C by securing the caps with suspended samples into the corrosion capsules and exposed for 500 h.

After 500 h of salt exposure, the copper and TZM samples were removed from the corrosion capsules while the salt was still at 700 °C and allowed to cool in the ultra-high purity argon glovebox atmosphere. Post-corrosion salt samples from all four capsules were collected by pouring the salt into 304 stainless steel cups. The salt solidified in <5 min ensuring that no significant additional corrosion products from the cups were introduced into the post-corrosion salt. To prepare the copper and TZM samples for post-corrosion analysis all samples were removed from the glovebox and cleaned to remove any residual FLiNaK by sonicating in 1 molar Al(NO<sub>3</sub>)<sub>3</sub> followed by ultrasonic cleaning in deionized water and acetone. The post-corrosion sample masses were then recorded using an electronic balance with 0.002 mg accuracy.

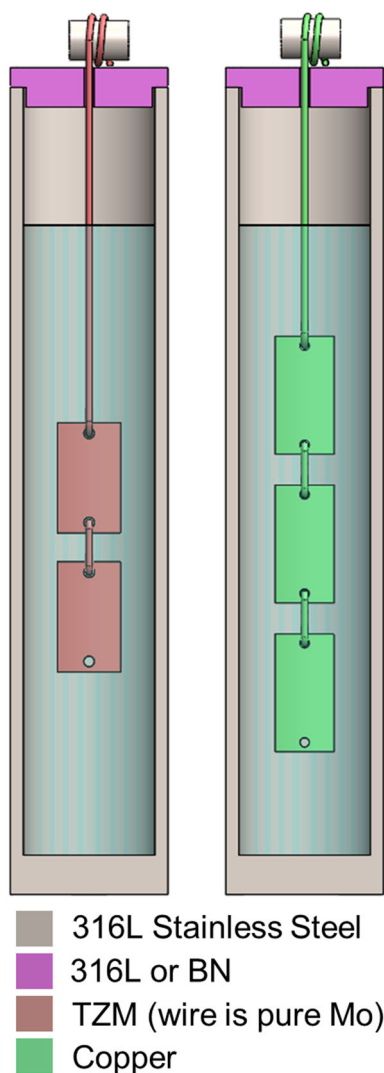


**Fig. 6 Schematic of the corrosion cell setup for the salt exposure of TZM and copper samples.** Two capsules with separate sample chains were tested such that in one capsule a 316L cap was used to create a galvanic couple between the 316L capsule and the sample chain and in the other capsule a BN cap was used so that the samples were electrically isolated from the 316L capsule.

### Post-corrosion analysis

X-ray diffraction (XRD) was performed on the uppermost sample from each capsule to identify any new phases that may have developed in the near-surface region. Surface SEM/EDS was also performed on the uppermost sample. XRD characterization was performed on a Bruker D8 Discovery using CuK- $\alpha$  x-rays and a Vantec 500 area detector with a 14 cm diameter active area. The bottom sample from each capsule was mounted and polished in cross-section for SEM/EDS analysis. All SEM/EDS was performed on a Zeiss LEO 1530 equipped with an energy dispersive x-ray spectrometer and Pathfinder software. For cross-sectional analysis on the two bottom TZM samples, the samples were electroplated with Cu after corrosion testing using a Cu-sulfate bath for edge retention during subsequent metallography steps. The two bottom post-corrosion copper samples were simply mounted in epoxy without applying a post-corrosion coating for edge retention. X-ray photoelectron spectroscopy (XPS) was performed on the uppermost TZM sample from the two TZM sample chains, while the middle sample from the two copper sample chains was used for identifying elements that would not be detectable by SEM-EDS analysis.

XPS measurements were performed using the Thermo k-alpha X-ray photoelectron spectrometer which is equipped with monochromatic Al k-alpha X-ray source for high energy resolution analysis with spot size of

approximately  $400 \times 600 \mu\text{m}^2$ . XPS analysis consisted of a survey scan from 0 to 1100 eV, then a scan over the Cu2p peak range of 925 to 965 eV, Ni2p range of 844 to 884 eV, Fe2p range of 700 to 740 eV, Mn2p range of 633 to 660 eV, Cr2p range of 570 to 595 eV, O1s range of 525 to 545 eV, Mo3d range of 222 to 242 eV, and Zr3d range of 174–194 eV. The XPS binding energy scales for the surface scan were corrected by setting the 1s orbital energy of adventitious carbon to 284.6 eV often used for carbon on metal surfaces<sup>39</sup>. XPSPEAK 4.1 software was used for fitting the XPS data<sup>40</sup>.

### DATA AVAILABILITY

The data that support the findings of this study are available from the corresponding author upon reasonable request.

### CODE AVAILABILITY

Code sharing is not available. Databases and software packages used in this study are products of Computherm, LLC.

Received: 27 October 2021; Accepted: 12 March 2022;

Published online: 19 April 2022

### REFERENCES

- Wright, R. N. & Sham, T.-L. *Status of Metallic Structural Materials for Molten Salt Reactors*. Idaho National Laboratory. Report No. INL/EXT-18-45171-Rev000 (2018).
- Xu, X. et al. Experimental test of properties of KCl–MgCl<sub>2</sub> eutectic molten salt for heat transfer and thermal storage fluid in concentrated solar power systems. *J. Sol. Energy Eng.* **140**, 051011 (2018).
- Vignarooban, K. et al. Vapor pressure and corrosivity of ternary metal-chloride molten-salt based heat transfer fluids for use in concentrating solar power systems. *Appl. Energy* **159**, 206–213 (2015).
- Sridharan, K. Understanding how materials corrode in nuclear reactors. *Adv. Mater. Process.* **170**, 17–20 (2014).
- Sridharan, K. & Allen, T. R. *Corrosion in Molten Salts* (Elsevier, 2013).
- Raiman, S. S., Muralidharan, G., Mayes, R. T. & Kurley, J. M. *Compatibility Studies of Cladding Candidates and Advanced Low-Cr Superalloys in Molten NaCl–MgCl<sub>2</sub>* (Oak Ridge National Lab, 2019).
- Falconer, C. et al. Non-galvanic mass transport in molten fluoride salt isothermal corrosion cells. *Corros. Sci.* **177**, 108955 (2020).
- Raiman, S. S. & Lee, S. Aggregation and data analysis of corrosion studies in molten chloride and fluoride salts. *J. Nucl. Mater.* **511**, 523–535 (2018).
- Doniger, W. H. et al. Investigation of impurity driven corrosion behavior in molten 2LiF–BeF<sub>2</sub> salt. *Corros. Sci.* **174**, 108823 (2020).
- Olson, L. C., Ambrosek, J. W., Sridharan, K., Anderson, M. H. & Allen, T. R. Materials corrosion in molten LiF–NaF–KF salt. *J. Fluor. Chem.* **130**, 67–73 (2009).
- Jones, D. A. *Principles and Prevention of Corrosion*. 2nd edn. (Prentice-Hall, Inc., 1996).
- Ai, H. et al. On the possibility of severe corrosion of a Ni–W–Cr alloy in fluoride molten salts at high temperature. *Corros. Sci.* **149**, 218–225 (2019).
- Dai, Q. et al. Corrosion of Incoloy 800H alloys with nickel cladding in FLiNaK salts at 850 °C. *Corros. Sci.* **133**, 349–357 (2018).
- Olson, L. C. et al. Impact of Corrosion Test Container Material in Molten Fluorides. *J. Sol. Energy Eng.* **137**, 061007 (2015).
- Ozeryanaya, I. N. Corrosion of metals by molten salts in heat-treatment processes. *Met. Sci. Heat. Treat.* **27**, 184–188 (1985).
- Wang, Y., Sridharan, K. & Couet, A. Method for identification of redox control parameters for corrosion mitigation in molten fluoride salts. *J. Nucl. Mater.* **543**, 152624 (2021).
- Baes, C. F. The chemistry and thermodynamics of molten salt reactor fuels. *Nucl. Metall.* **15**, 617–644 (1969).
- Wang, Y. & Zhang, J. Electrochemical properties of CrF<sub>2</sub> in FLiNaK molten salt and the new analytical methods for their determination. *J. Electrochem. Soc.* **167**, 086503 (2020).
- Peng, H. et al. Electrochemical investigation of the stable chromium species in molten FLiNaK. *RSC Adv.* **5**, 76689–76695 (2015).
- Snyder, R. B., Natesan, K. & Kassner, T. F. *Analysis of Carbon Transport in the EBR-II and FFTF Primary Sodium Systems*. Report No. CONF-760503-12 (Argonne National Lab, 1976).
- Sannier, J., Paidassi, J., Dixmier, J., Leclercq, D. & Konovaltschikoff, O. Decarburation des aciers ferritiques dans le sodium en circulation entre 475 et 550 °C. *J. Nucl. Mater.* **55**, 169–176 (1975).

22. HSC Chemistry 7 v. 7.00 (Outotec Research Oy, 2009). [www.outotec.com/hsc](http://www.outotec.com/hsc).
23. PanHEA Database v. 2021 (CompuTherm, LLC, 2021). [www.computherm.com](http://www.computherm.com).
24. PanNickel Database v. 2021 (CompuTherm, LLC, 2021). [www.computherm.com](http://www.computherm.com).
25. Ai, H. et al. Influence of graphite-alloy interactions on corrosion of Ni-Mo-Cr alloy in molten fluorides. *J. Nucl. Mater.* **503**, 116–123 (2018).
26. Pandat v. 2020 (CompuTherm, LLC, 2020). [www.computherm.com](http://www.computherm.com).
27. Koger, J. W. & Litman, A. P. *Compatibility of Molybdenum-base Alloy TZM with LiF-BE2-ThF4-UF4 (68-20-11.7-0.3 mole %) at 1100 °C*. Report No. ORNL-TM-2724 (Oak Ridge, Tennessee, 1969).
28. Weiss, B. & Stickler, R. Phase instabilities during high temperature exposure of 316 austenitic stainless steel. *METALL MATER TRANS B* **3**, 851–866 (1972).
29. Elbakhshwan, M. et al. Corrosion and thermal stability of CrMnFeNi high entropy alloy in molten FLiBe salt. *Sci. Rep.* **9**, 18993 (2019).
30. Guillermet, A. F. An assessment of the Fe-Mo system. *Calphad* **6**, 127–140 (1982).
31. Poulouse, A. C. et al. Multifunctional Cu<sub>2</sub>-xTe nanocubes mediated combination therapy for multi-drug resistant MDA MB 453. *Sci. Rep.* **6**, 35961 (2016).
32. Meškinis, Š. et al. Hydrogen-free diamond like carbon films with embedded Cu nanoparticles: structure, composition and reverse saturable absorption effect. *Mater. (Basel)* **13**, 760 (2020).
33. Heijleggen, G. P. & Rieck, G. D. Diffusion in the Mo-Ni, Mo-Fe and Mo-Co systems. *Acta Met.* **22**, 1269–1281 (1974).
34. Williams, D., Toth, L. & Clarno, K. *Assessment of Candidate Molten Salt Coolants for the Advanced High-Temperature Reactor (AHTR)*. Report No. ORNL/TM-2006/12, (Oak Ridge National Lab., 2006).
35. Marković, B. et al. Experimental study and thermodynamic remodeling of the Bi-Cu-Ni system. *Calphad* **34**, 294–300 (2010).
36. Weinstein, M. et al. Environmental degradation of electroplated nickel and copper coated SS316H in molten FLiNaK salt. *Corros. Sci.* **191**, 109735 (2021).
37. Chen, S. L. et al. The PANDAT software package and its applications. *Calphad* **26**, 175–188 (2002).
38. Cao, W. et al. PANDAT software with PanEngine, PanOptimizer and PanPrecipitation for multi-component phase diagram calculation and materials property simulation. *Calphad* **33**, 328–342 (2009).
39. Stumpf, S. et al. Development of fuel-model interfaces: Investigations by XPS, TEM, SEM and AFM. *J. Nucl. Mater.* **385**, 208–211 (2009).
40. XPSPEAK 4.1 (2000). [www.xpspeak.software.informer.com/4.1/](http://www.xpspeak.software.informer.com/4.1/).

## ACKNOWLEDGEMENTS

This work was partially funded under an IRP grant (Grant No. DE-NE0008651) from the United States Department of Energy, Office of Nuclear Energy, as well as NEUP grants (Grant Nos. DE-NE0008802 and DE-NE0008803) from the United States Department of Energy. Any opinions, findings, conclusions, or recommendations expressed in this publication are those of the author(s) and do not necessarily reflect the views of the Department of Energy, Office of Nuclear Energy. The authors gratefully acknowledge use of facilities and instrumentation at the UW-Madison Wisconsin Centers for Nanoscale Technology ([wcnt.wisc.edu](http://wcnt.wisc.edu)) partially supported by

the NSF through the University of Wisconsin Materials Research Science and Engineering Center (DMR-1720415). Special thanks to Chuan Zhang and CompuTherm LLC for assistance with the Pandat Software and associated databases.

## AUTHOR CONTRIBUTIONS

C.F. conceived the subject of this study and performed the molten salt exposures alongside W.D. and M.W. M.E. performed the XPS investigation. C.F. performed the activity modeling calculations, XRD, and SEM analysis. C.F., M.E., and A.C. drafted the original manuscript. W.D., M.W., and K.S. assisted in the manuscript review. A.C. and K. S. provided guidance over the methodology and provided funding for the work. All authors contributed to the interpretation of the post-corrosion data analysis.

## COMPETING INTERESTS

The authors declare no competing interests.

## ADDITIONAL INFORMATION

**Supplementary information** The online version contains supplementary material available at <https://doi.org/10.1038/s41529-022-00239-z>.

**Correspondence** and requests for materials should be addressed to Cody Falconer.

**Reprints and permission information** is available at <http://www.nature.com/reprints>

**Publisher's note** Springer Nature remains neutral with regard to jurisdictional claims in published maps and institutional affiliations.



**Open Access** This article is licensed under a Creative Commons Attribution 4.0 International License, which permits use, sharing, adaptation, distribution and reproduction in any medium or format, as long as you give appropriate credit to the original author(s) and the source, provide a link to the Creative Commons license, and indicate if changes were made. The images or other third party material in this article are included in the article's Creative Commons license, unless indicated otherwise in a credit line to the material. If material is not included in the article's Creative Commons license and your intended use is not permitted by statutory regulation or exceeds the permitted use, you will need to obtain permission directly from the copyright holder. To view a copy of this license, visit <http://creativecommons.org/licenses/by/4.0/>.

© The Author(s) 2022